

CSF circulation and dispersion yield rapid clearance from intracranial compartments

Martin Hornkjøl¹, Lars Magnus Valnes³, Geir Ringstad^{5,6}, Marie E. Rognes^{2, 4}, Per-Kristian Eide^{3,7}, Kent-André Mardal^{1, 2}, and Vegard Vinje²

¹Department of Mathematics, University of Oslo, Blindern, Norway

²Department of Numerical Analysis and Scientific Computing, Simula Research Laboratory, Kristian Augusts gate 23, 0134 Oslo, Norway

³Department of Neurosurgery, Oslo University Hospital–Rikshospitalet, Nydalen, PB 4950, 0424 Oslo, Norway

⁴Department of Mathematics, University of Bergen, PB 7803, 5020 Bergen, Norway

⁵Department of Radiology, Oslo University Hospital, Oslo, Norway

⁶Department of Geriatrics and Internal Medicine, Sorlandet Hospital, Arendal, Norway

⁷Institute of clinical medicine, Faculty of medicine, University of Oslo, Oslo, Norway

ABSTRACT

In this paper we used a computational model to estimate the clearance of tracer driven by circulation of cerebrospinal fluid (CSF) produced in the choroid plexus (CP) located within the lateral ventricles. CSF was assumed to exit the subarachnoid space (SAS) via different outflow routes such as the parasagittal dura, cribriform plate and/or meningeal lymphatics. We also modelled a reverse case where fluid was produced within the spinal canal and absorbed in the CP in line with observation on certain iNPH patients. No directional interstitial fluid flow was assumed within the brain parenchyma. Tracers were injected into the foramen magnum. The models demonstrate that convection in the SAS yield rapid clearance from both the SAS and the brain interstitial fluid (ISF) and can speed up intracranial clearance from years, as would be the case for purely diffusive flow, to days.

Keywords: mathematical modelling, CSF dynamics, subarachnoid space, convection-diffusion, clearance, glymphatics

1 Introduction

Cerebrospinal fluid (CSF) flow plays a fundamental role in the clearance of solutes from intracranial compartments^{1,2}. Current views postulate that CSF is primarily produced in the choroid plexus^{1,3}, and flows through the ventricular system⁴⁻⁶ and along the subarachnoid space (SAS)⁷⁻⁹. From there, CSF drains towards the venous system via arachnoid granulations¹⁰, towards lymph nodes via e.g. perineural routes across the cribriform plate^{2,7,11} or the meningeal lymphatics¹², or flows through the brain parenchyma itself via glymphatic (perivascular) pathways¹³. The relative importance of these pathways, their interplay, and role(s) in physiological as well as pathological solute transport remain unresolved^{1,2,7,8,10,12,14}.

Importantly, CSF circulation characteristics change under physiological transitions, in neurological disorders and with neurodegenerative disease. In patients diagnosed with idiopathic normal pressure hydrocephalus (iNPH), MR-imaging reveals altered solute influx and clearance rates¹⁵. In both Alzheimer's and iNPH patients, CSF dynamics in the SAS is altered^{15,16}, and CSF production within the choroid plexus may be reduced in iNPH⁶. On the other hand, changes in glymphatic function may be associated with several types of dementia¹⁷. In Alzheimer's disease, alterations in arterial pulsatility¹⁸, AQP4 function¹⁹ and sleep disturbances²⁰ has been proposed as causes of glymphatic impairment. Lastly, glymphatic transport has been reported to increase during sleep^{21,22}.

A key question is to what extent the CSF circulation induced by CSF production, vascular pulsatility and CSF efflux contributes to transport of solutes (both influx and outflux) in the SAS and brain parenchyma. While intraparenchymal transport and glymphatics have received substantial attention over the last decade^{1,13,14,21-29}, the clearance interplay between different regions within the intracranial compartment is less understood. To illustrate,

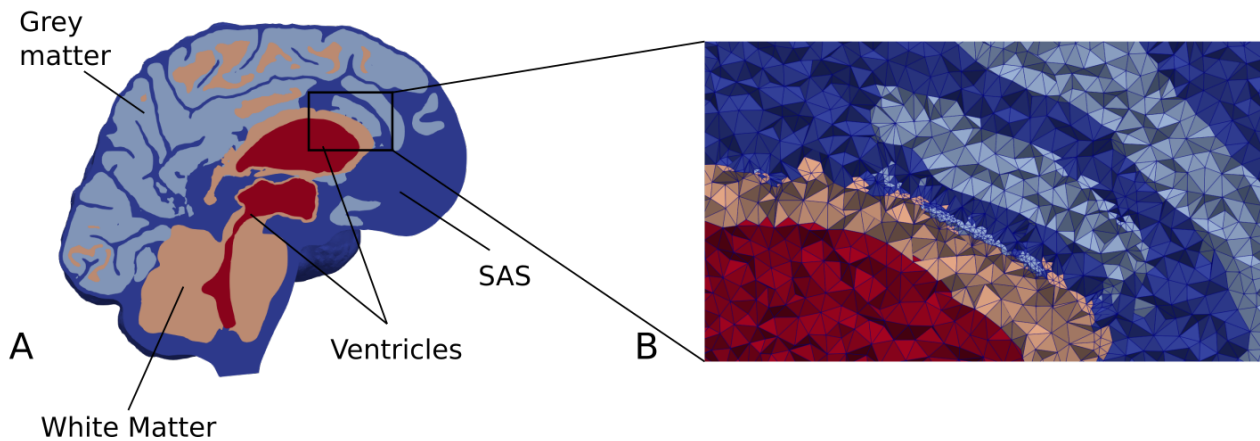


Figure 1. (A) A cross section of our brain mesh showing the SAS (dark blue), white matter (orange), gray matter (light blue), ventricles (red), (B) shows a zoom in on a part of the mesh with the edges of the mesh triangles. Note that for visualization purposes, the resolution shown here is coarser than the resolution used in the numerical simulations.

34 while Xie et al²¹ suggest that the sleep-wake cycle regulates the efficiency of glymphatic solute clearance via changes
35 in the interstitial space volume, the findings of Ma et al⁷ offer an alternative interpretation in which increased
36 CSF outflow during wakefulness effectively limits the availability of solutes at the surface and within parenchymal
37 perivascular spaces (PVSs). As the intracranial CSF volume is only 10–30% that of the brain^{30,31}, rapid clearance of
38 substances from the SAS is crucial to sustain diffusive transport from the brain parenchyma to the SAS.

39 Crucially, CSF flow velocities in the SAS, including in surface PVSs, are substantial. Pulsatile CSF velocities
40 of at least 10–40 $\mu\text{m/s}$ can be inferred from experimental measurements of microsphere movement in rodents^{8,9}.
41 Furthermore, the resulting dispersion effects may dominate diffusion by a factor of 10^4 for transport of smaller
42 molecules such as the MRI contrast molecule Gadoteridol²⁹. In humans, CSF flow in the SAS varies significantly
43 between patients and diseases³², with velocities at the foramen magnum induced by pulsatile flow on the order of 5
44 cm/s ³³. Interestingly, CSF bulk flow at a magnitude of $\mu\text{m/s}$ can be induced in the ventricular system and surface
45 PVSs by relatively small intracranial pressure gradients ($< 1\text{--}2 \text{ mmHg/m}$)³⁴.

46 In this study, using biophysics-based finite element computational models created from T1- and T2-weighted
47 MR images^{15,35}, we study CSF flow in the ventricular system and SAS and solute transport in these CSF-filled
48 spaces and brain parenchyma. We first simulate flow patterns and magnitude induced by a production of 0.5L CSF
49 per day³⁶ in the choroid plexus and different CSF efflux pathways: across the parasagittal dura, across the cribriform
50 plate, and into meningeal lymphatics, as well as reversed flow scenarios. We next simulate solute transport in the
51 SAS and brain parenchyma resulting from an intrathecal injection of Gadobutrol. Our findings indicate that CSF
52 flow in the SAS is a major player in brain clearance. However, no single outflow pathway alone is able to explain
53 in-vivo observations of brain-wide distribution of tracer combined with fast clearance from the SAS, and we thus
54 propose that a combination of different outflow routes seem more likely.

55 2 Methods

56 In this computational study, we quantify and characterize CSF flow patterns and molecular transport in the SAS and
57 parenchyma induced by different clearance pathways. We also consider a choroid plexus-based production of 0.5
58 L/day of CSF and efflux across the 1) parasagittal dura³⁷, 2) the cribriform plate¹¹, and 3) meningeal lymphatics¹².
59 We consider a scenario with retrograde flow in the aqueduct⁴ by assuming that 0.5 L/day CSF production occurs
60 within the spinal cord and as such that there is an influx through the foramen magnum, combined with an efflux route
61 in the choroid plexus. An illustration of a slice of the computational domain is given in Figure 1.

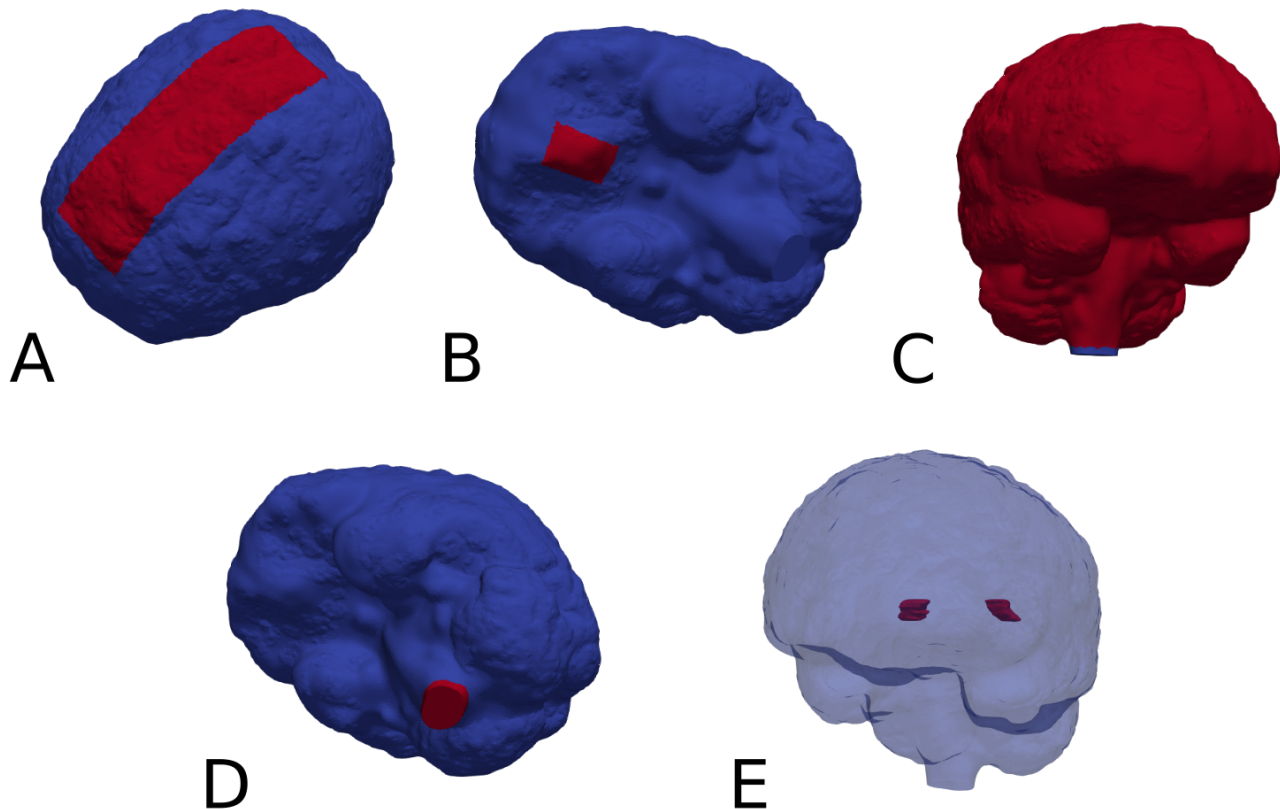


Figure 2. Red markers highlight important subregions and boundaries in the computational domain: the (A) parasagittal dura, (B) cribriform plate, (C) meningeal lymphatics, (D) foramen magnum and (E) choroid plexus.

62 2.1 Patient data and approvals

63 We consider baseline T1- and T2-weighted MR images (resolution 1 mm) from an iNPH patient collected in a
64 previous clinical study. This patient then also underwent a (0.5 ml, 1 mmol/ml) intrathecal injection of gadobutrol,
65 and follow-up MR images were taken at several time points post injection. LookLocker images were also obtained
66 with the T1-weighted MR images. The clinical study was approved by the Regional Committee for Medical and
67 Health Research Ethics (REK) of Health Region South-East, Norway (2015/96), the Institutional Review Board of
68 Oslo University Hospital (2015/1868), the National Medicines Agency (15/04932-7), and conducted in accordance
69 with the ethical standards of the Declaration of Helsinki of 1975 (and as revised in 1983). All study participants
70 were included after written and oral informed consent.

71 2.2 In-vivo imaging concentration estimates

72 The baseline MR images were post-processed using FreeSurfer v6.0³⁸ to obtain a segmentation of the brain. To
73 define a choroid plexus (CP) completely enclosed by the lateral ventricles, a CP domain was manually marked in the
74 images. Next, the left and right pial membrane, white matter interface, cerebellum, ventricles and aqueduct were
75 represented via triangulated surfaces. The segmentation of the SAS was performed by thresholding a registered
76 T2-weighted image, and any clusters not connected to the FreeSurfer segmentation were removed. Subsequently, a
77 surface bounding the SAS was constructed, and expanded by 1 mm in the surface normal direction to ensure that
78 the SAS was represented as a continuous compartment between the pia and dura around the whole brain. The CSF
79 volume before and after expansion were 457 and 602 mL, respectively. The spinal cord was not segmented, and was
80 represented as CSF for simplicity. The parenchymal volume was 1266 mL. Both the CSF and parenchymal volumes
81 are slightly above average values in iNPH patients³¹.

82 The generated surfaces were further post-processed using SVMTK³⁹, and finally used to generate a volumetric

83 mesh Ω of the parenchyma Ω_P and surrounding CSF-spaces Ω_F combined (Figure 1). We label the boundary
 84 separating Ω_P and Ω_F by $\partial\Omega_P$. The choroid plexus $\Omega_{CP} \subset \Omega_F$ is located within the lateral ventricles and we denote
 85 its surface (in contact with the CSF) by $\partial\Omega_{CP}$. The outer boundary of the SAS is split into three parts: $\partial\Omega_S$, $\partial\Omega_{FM}$,
 86 and $\partial\Omega_{out}$, representing the arachnoid membrane, foramen magnum and a chosen efflux route, respectively. We
 87 consider and define three different regions Ω_{out} for efflux of CSF: locally across the *parasagittal dura* (Figure
 88 2A), locally across the *cribriform plate* (Figure 2B), or into the meningeal *lymphatics* distributed over the outer
 89 (arachnoid) boundary (Figure 2C). Finally, to simulate retro-grade net aquaductal flow, we consider flow into the
 90 choroid plexus (Figure 2E) from the foramen magnum (Figure 2D).

91 2.3 Flow in the CSF spaces

We model the flow of CSF in Ω_F by the incompressible Stokes equations: find the CSF velocity field u and pressure p such that

$$\mu \nabla^2 u - \nabla p = 0 \quad \text{in } \Omega_F, \quad (1a)$$

$$\nabla \cdot u = g \quad \text{in } \Omega_F, \quad (1b)$$

92 where g is a given source of fluid. With the low Reynolds numbers (0.001) reported for flow in PVS^{9,40}, we find
 93 steady Stokes flow to be a reasonable assumption for the present study. To represent CSF production in the choroid
 94 plexus, we let g be a given positive constant in Ω_{CP} and zero elsewhere in Ω_F . Specifically, by default, we set
 95 g such that approximately 0.5L of CSF is produced every 24 hours. We also consider a scenario with increased
 96 CSF-production. In humans, the CSF production has been reported to increase during sleep^{41,42}, while high CSF
 97 turnover through lymphatics has been reported in awake mice⁷. We set the parenchymal CSF/brain interstitial fluid
 98 (ISF) velocity to be zero (in Ω_P).

We set the CSF velocity at the outer boundary (representing the arachnoid membrane) to be zero, except at
 specific efflux/absorption sites $\partial\Omega_{out}$ to be further specified. At these, we set a traction condition:

$$\mu \nabla u \cdot n - pn = -R_0 u \cdot n \quad \text{on } \partial\Omega_{out}, \quad (2)$$

99 where $R_0 \geq 0$ represents an efflux resistance acting to moderate CSF outflow in these regions, and n denotes the
 100 outward pointing boundary normal. The fluid source, in combination with the zero or low resistance efflux routes,
 101 induces a flow of CSF from the CP through the ventricular system, through the SAS and out across either the
 102 parasagittal dura, cribriform plate, or meningeal lymphatics.

103 We also consider a reversed flow scenario, in which g is set negative with a value corresponding to a sink of 0.5
 104 L/day, a zero traction condition is imposed at the foramen magnum $\partial\Omega_{FM}$, and zero velocity (no slip) is imposed on
 105 the remainder of the boundary.

106 2.4 Molecular transport in the CSF and parenchyma

We also model molecular transport within the CSF-spaces and parenchyma resulting from an influx of gadobutrol at
 the foramen magnum (resulting e.g. from an intrathecal injection). We model transport of a concentration c in the
 entire domain Ω via the diffusion-convection equation:

$$\phi \frac{\partial c}{\partial t} + \phi u \cdot \nabla c - \nabla \cdot (\phi \alpha D \nabla c) = 0 \quad \text{in } \Omega, \quad (3)$$

107 where u is a convective velocity field, D denotes an apparent diffusion coefficient, and α is a dispersion factor.
 108 We set the apparent diffusion coefficients $D_F = 3.8 \cdot 10^{-4}$ mm²/s in Ω_F and $D_P = \frac{D_F}{\lambda^2} = 1.2 \cdot 10^{-4}$ mm²/s in Ω_P ²⁸.
 109 Here, $\lambda \approx 1.78$, represents the tortuosity. To represent enhanced diffusion in the CSF due to pulsatile effects,
 110 mixing or other forms of dispersion^{23,29,43}, we have introduced the dispersion factor α , and consider a range of
 111 $\alpha \in \{1, 10, 100, 1000\}$ in Ω_F . In Ω_P we set $\alpha = 1$. ϕ accounts for the porosity of the extracellular space which
 112 occupies 20 % of the parenchyma⁴⁴, and we thus set $\phi_P = 0.2$ and $\phi_F = 1$. We consider either $u = 0$ and $\alpha = 1$
 113 (diffusion-only scenarios) or let u be given by solutions of the CSF flow equations (1) in combination with all α .

Model	Production site	Absorption site	R_0 (Pa/(mm s))	β (mm ² /s)	Production (L/day)
I	Choroid plexus	Parasagittal dura	0	∞	0.5
II	Choroid plexus	Cribriform plate	0	∞	0.5
III	Choroid plexus	Parasagittal dura	0	10^{-4}	0.5
IV	Choroid plexus	meningeal lymphatics	10^{-5}	10^{-4}	0.5
V	Foramen magnum	Choroid plexus	0	∞	0.5
VI	Choroid plexus	Cribriform plate	0	∞	1.0

Table 1. Overview of computational models. Production and absorption site refers to production site for CSF and efflux/absorption site of CSF and the solute concentration, respectively. R_0 is a CSF efflux resistance parameter cf. (2), while β represents a diffusive resistance to molecular efflux cf. (6). The values for R_0 and β were estimated by numerical experimentation.

To represent an influx of gadobutrol at the foramen magnum, we set

$$D\nabla c \cdot n - cu \cdot n = F(t) \quad \text{on } \partial\Omega_{\text{FM}}. \quad (4)$$

Based on tracer enhancement as reported by Eide et al.⁶, $F(t)$ is modeled as a linearly decreasing function until $T_0 \approx 2.24$ hours (8064 s) and zero thereafter i.e.

$$F(t) = \begin{cases} 2.395 \cdot 10^{-11} (T_0 - t) & \text{if } t < T_0 \\ 0 & \text{otherwise.} \end{cases} \quad (5)$$

The solute influx $F(t)$ (given in mmol/(s mm²)) is chosen such that the total amount of gadobutrol injected is approximately 0.5 mmol. At the efflux sites $\partial\Omega_{\text{out}}$, we let the solute be absorbed via the relation

$$D\nabla c \cdot n - cu \cdot n = -\beta c \quad \text{on } \partial\Omega_{\text{out}}, \quad (6)$$

where β is a given membrane permeability. The case $\beta = 0$ corresponds to no absorption, $\beta = \infty$ corresponds to free movement of solutes across the boundary, while $0 < \beta < \infty$ represents a diffusive resistance to molecular outflow. On the remainder of the boundary, we do not allow for solute efflux, by setting $D\nabla c \cdot n - cu \cdot n = 0$. Moreover, we let the initial concentration be $c(x, 0) = 0$. Note that to model transport associated with the reversed flow scenario, we let $\partial\Omega_{\text{CP}}$ take the role of $\partial\Omega_{\text{out}}$.

At the interface between Ω_F and Ω_P we conserve mass (enforce conservation of molecules) by setting $\phi D_P \nabla_{CP} \cdot n = D_F \nabla_{CF} \cdot n$. Here, D_P and D_F denote D restricted to Ω_P and Ω_F , respectively, n is the normal vector on the interface, pointing from Ω_P to Ω_F and ϕ denotes the ECS porosity.

2.5 Overview of models

CSF and solutes may have several simultaneous and possibly partially independent outflow routes². We here consider six different flow and transport models separately (Table 1), each with different dispersion factors. This design allows us to systematically examine different pathways and evaluate whether each or combinations could describe in-vivo observations of Gadobutrol transport. Model I and II describe flow induced by CSF production in the CP, and CSF efflux across the parasagittal dura and cribriform plate, respectively. For these models, we assume free molecular efflux at the absorption sites. Model III is a variant of Model I with a finite molecular efflux permeability at the parasagittal dura absorption site. Model IV reflects a different efflux pathway with CSF production in the CP, CSF efflux into the meningeal lymphatics, and a finite molecular efflux permeability. Model V represents a reversed flow scenario with absorption of CSF in the CP region (and CSF influx at the foramen magnum). Finally, Model VI represents a variant of Model II with increased CSF production.

133 2.6 Numerical methods, simulation software and verification

134 The Stokes equations are solved using a finite element method with Taylor-Hood (continuous piecewise quadratic
135 and continuous piecewise linear) elements for the velocity and pressure. The diffusion-convection equation with
136 boundary conditions is solved numerically using the finite element method with continuous linear finite elements for
137 the concentration in space, and the backward Euler method in time; all using the FEniCS finite element software^{45,46}.
138 The brain mesh has 6 691 432 cells and 1 088 640 vertices. The degrees of freedom for the diffusion equation
139 is equal to the number of vertices. For the Taylor-Hood case the number of degrees of freedom is 27 858 018.
140 Moreover, the largest cell size is 2.4 mm and the smallest is 0.07 mm. The largest cells are in the middle of white
141 matter where there are no stokes flow or sharp gradients.

142 A time resolution study was performed to ensure that our simulation results were independent of the choice
143 of time step (Supplementary Figure S1). Including testing and validation, a total of $\approx 30,000$ CPU hours was
144 used to run the simulations on big memory nodes. All simulations were run on the high-performance computing
145 infrastructure Sigma2 – the National Infrastructure for High Performance Computing and Data Storage in Norway.

146 2.7 Concentration estimates from in-vivo MRI

We extract contrast agent concentration estimates from the MR images post injection for comparison with computa-
tional predictions. The contrast agent shortens the T1 times as:

$$\frac{1}{T_1(c)} = r_1 c + \frac{1}{T_1(0)}, \quad (7)$$

147 where c denotes the concentration of the contrast agent, r_1 is known as the T1 relaxivity of the agent, and $T_1(c)$ and
148 $T_1(0)$ denote the T1 time with and without concentration, respectively. The T1 times can be computed using a T1
149 mapping⁴⁷, such as the LookLocker sequence. Through a preliminary phantom study, the relaxivity constant for this
150 LookLocker protocol was found to be $6.5 \text{ L mmol}^{-1} \text{ s}^{-1}$. The median T1 time over the parenchyma was used in
151 (7) to estimate the concentration in the parenchyma. The CSF concentration was estimated by manually creating a
152 region of interest (ROI) in the CSF, and using the average T1 time over the ROI with (7). Finally, to transform the
153 concentration in the parenchyma to be that of the the extracellular space, the concentrations was multiplied by five.

154 2.8 Quantities of interest

The total amount of solute in a given region Ω_i ($i = F, P$) at time t was computed as $M_i(t) = \int_{\Omega_i} \phi_i c dx$. The total
amount within the intracranial compartment $M(t)$ is then the sum $M(t) = M_P(t) + M_F(t)$. The average concentrations
per region over time were computed as

$$\bar{c}_i = \frac{M_i(t)}{\phi_i V_i},$$

155 where V_i refers to the volume of the respective region. To compare parenchymal influx between models, we compute
156 the peak average concentration in the parenchyma and the time to reach this peak. We also compute the relative
157 clearance of tracers after $T_1 = 3$ days as $1 - \frac{M(T_1)}{M(0)}$.

158 3 Results

159 All models induce non-trivial CSF flows through the ventricular system and subarachnoid space.

160 3.1 Different outflow routes induce different CSF flow patterns and velocities

161 Models I–IV all reach maximal SAS velocities of 8.9 mm/s in the thinnest part of the aqueduct (Figure 3A–C).
162 Despite their differences in efflux pathways, all of these models predict higher CSF flow velocities in the anterior
163 regions of the SAS compared to posterior regions. Model II displays the highest velocities in the SAS, reaching 50
164 $\mu\text{m/s}$. Model I (and III) reaches peak CSF velocities of 40 $\mu\text{m/s}$. In model IV, CSF flow occurs mainly in the lower
165 regions of the SAS as CSF can exit the SAS along the entire boundary. Peak velocities in the SAS for model IV

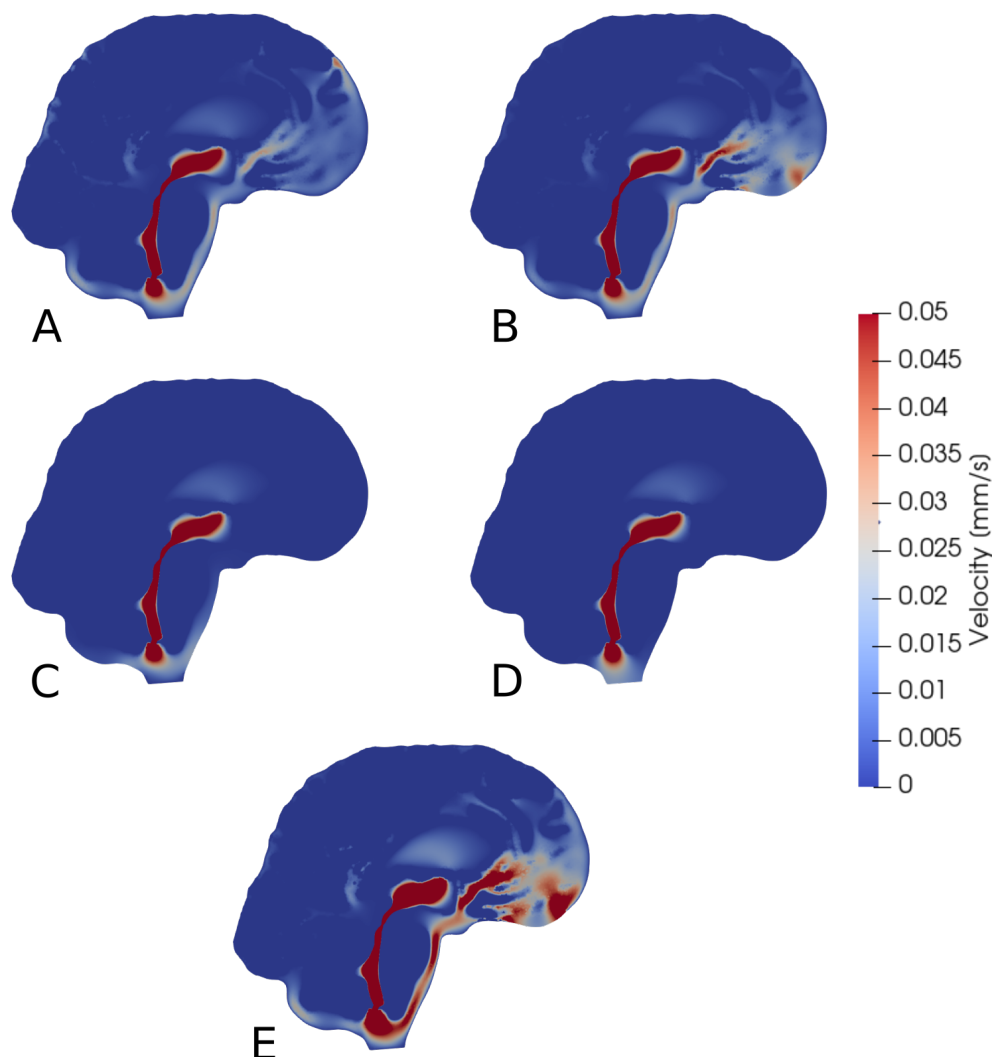


Figure 3. Sagittal views (cut through the center of the aqueduct) of CSF velocity magnitudes induced by steady CSF production in the choroid plexus combined with different CSF efflux pathway models, or a reversed flow scenario. Subfigures show velocity fields resulting from CSF efflux through (A) the parasagittal dura, (B) the cribriform plate, (C) the meningeal lymphatics (D) production in the foramen magnum and absorption in the choroid plexus, or (E) the cribriform plate with double production. The color map is capped at 0.05 mm/s for visualization purposes.

		Time to par peak (hours)				Three day clearance rate (%)				Peak avg par conc (mmol/L)			
M	α	1	10	100	1000	1	10	100	1000	1	10	100	1000
	I		19.0	15.7	14.6	7.8	95.6	94.1	94.4	97.7	0.18	0.27	0.30
II		16.8	12.3	12.3	10.1	94.0	91.2	88.9	94.9	0.07	0.12	0.17	0.24
III		20.2	19.0	22.4	35.8	95.7	91.3	82.8	36.3	0.14	0.32	0.43	0.50
IV		12.3	17.9	15.7	11.2	99.0	89.5	91.5	94.0	0.01	0.13	0.19	0.23
V		>72	22.4	10.8	19.0	75.1	86.9	90.0	82.6	0.12	0.07	0.09	0.18
VI		11.2	9.0	7.8	7.8	97.9	95.5	95.4	97.4	0.05	0.08	0.11	0.18

Table 2. The table shows time to peak concentration in the parenchyma (left), total mass clearance in the intracranial compartment after 72 hours (middle) and peak average concentration values in the parenchyma (right) for the case of gadobutrol transport. Values are shown for all models and α values. M: Model, α : Dispersion factor, par: parenchyma, conc: concentration, avg: average

166 reach 20 $\mu\text{m/s}$. In models where CSF was allowed to exit through outflow routes other than the parasagittal dura
 167 (models II and IV), CSF velocity magnitudes were relatively small ($< 4 \mu\text{m/s}$) in the SAS near the upper convexities
 168 of the brain.

169 3.2 Reversed CSF flow pathways

170 Model V predicts that, under its assumptions, CSF will predominantly flow from the foramen magnum directly to
 171 the CP, limiting CSF flow in other parts of the SAS (Figure 3D). thus the flow direction is reversed compared to
 172 models I–IV. In the foramen magnum, CSF velocity magnitudes reach 20 $\mu\text{m/s}$, while the velocity in the aqueduct
 173 remain at 8.9 mm/s. In the upper regions of the SAS, not directly associated with the 3rd ventricle, CSF velocities
 174 were typically lower than 0.1 $\mu\text{m/s}$.

175 3.3 Increased CSF production increase CSF velocities

176 Doubling the CSF production (model VI versus model II) results in a doubling of the CSF velocity field by linearity.
 177 Therefore, we observe velocities of approx. 100 $\mu\text{m/s}$ in the CSF space (Figure 3E) and a velocity in the aqueduct of
 178 17.8 mm/s for model VI.

179 3.4 Diffusion alone yields excessively slow clearance from intracranial compartments

180 When driven purely by diffusion (without convection or dispersion enhancements), the tracer spreads radially from
 181 the foramen magnum and distributes evenly throughout the brain. Distribution is slightly faster in the CSF than in
 182 the parenchyma, as the free diffusion coefficient in CSF is larger. However, this effect is not very noticeable. For
 183 Models I–III the relative one year clearance is only 32.8 %, 17.6 % and 29.9 %. Model IV displays faster clearance,
 184 clearing 92.5 % over one week, but with a late peak parenchyma concentration occurring after 79 hours.

185 3.5 Tracer distribution patterns induced by CSF circulation and dispersion

186 Including the CSF circulation-induced flow as a convective velocity substantially speeds up the clearance rates, both
 187 from the SAS and parenchyma.

188 Tracer distribution is shown for all models after 6 and 24 hours and $\alpha = 10$ in Figure 4, revealing substantial
 189 inter-model variations. For Model I, the tracer is mainly confined to the SAS and moves upwards towards the
 190 parasagittal dura showing a clear preference traveling along the SAS in the right hemisphere (data not shown).
 191 As there is no molecular resistance to outflow on the parasagittal dura in Model I, tracer is instantly
 192 transported out when moving into this efflux route. In regions where the tracer concentration in the SAS is high, the
 193 tracer also enters the brain due to the large concentration gradient between the SAS and the brain (4A, B Model I).

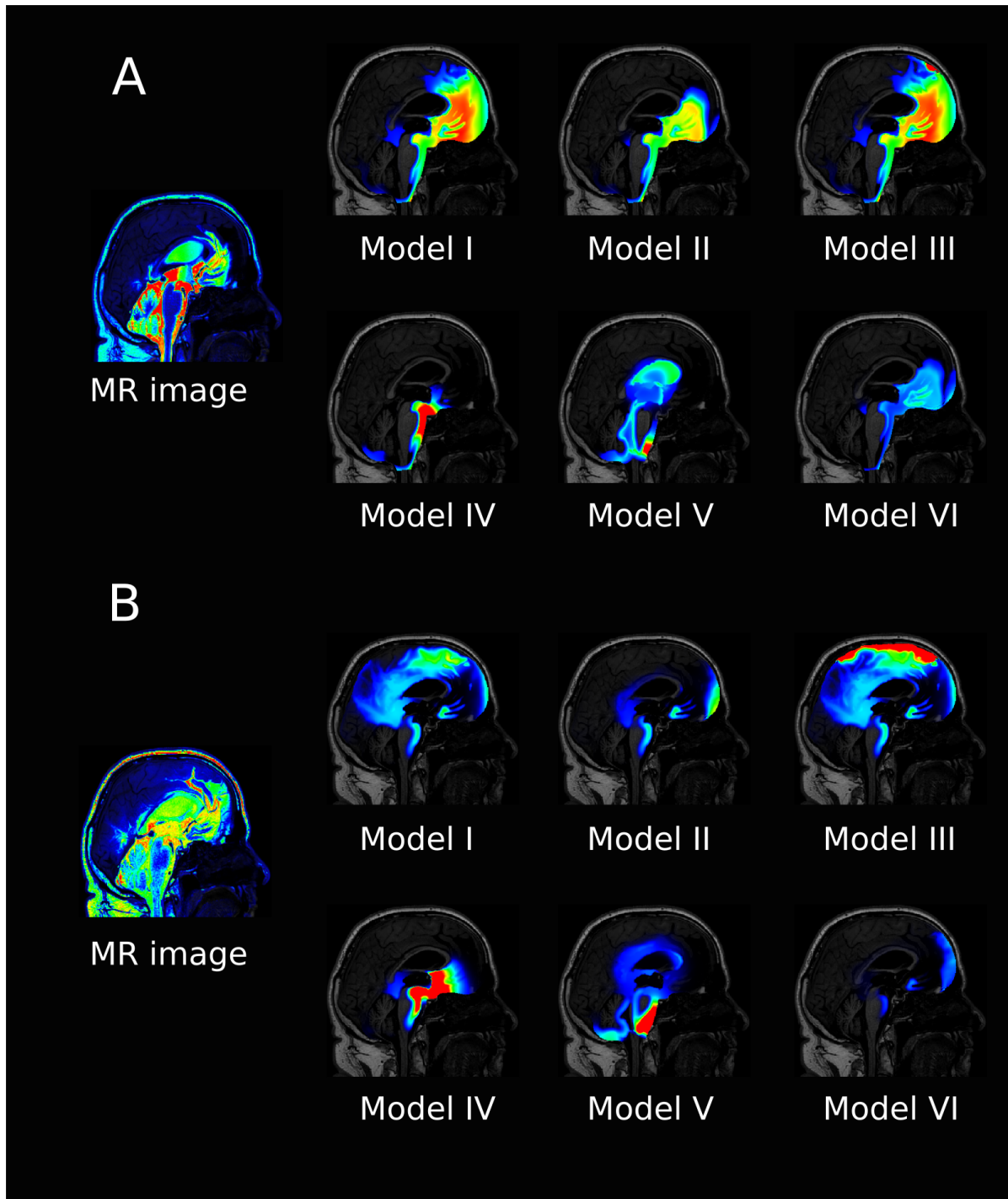


Figure 4. The figure shows a sagittal view of all the models at 6 hours (A) and 24 hours (B) after intrathecal injection of gadobutrol for $\alpha = 10$. For the simulation data, the colorscale shown is 0.1–5 mmol/L in A and 0.1–1 mmol/L in B. For comparison the T1 contrast enhanced image for the patient at the same times are included. The MR images are scaled separately for picture legibility.

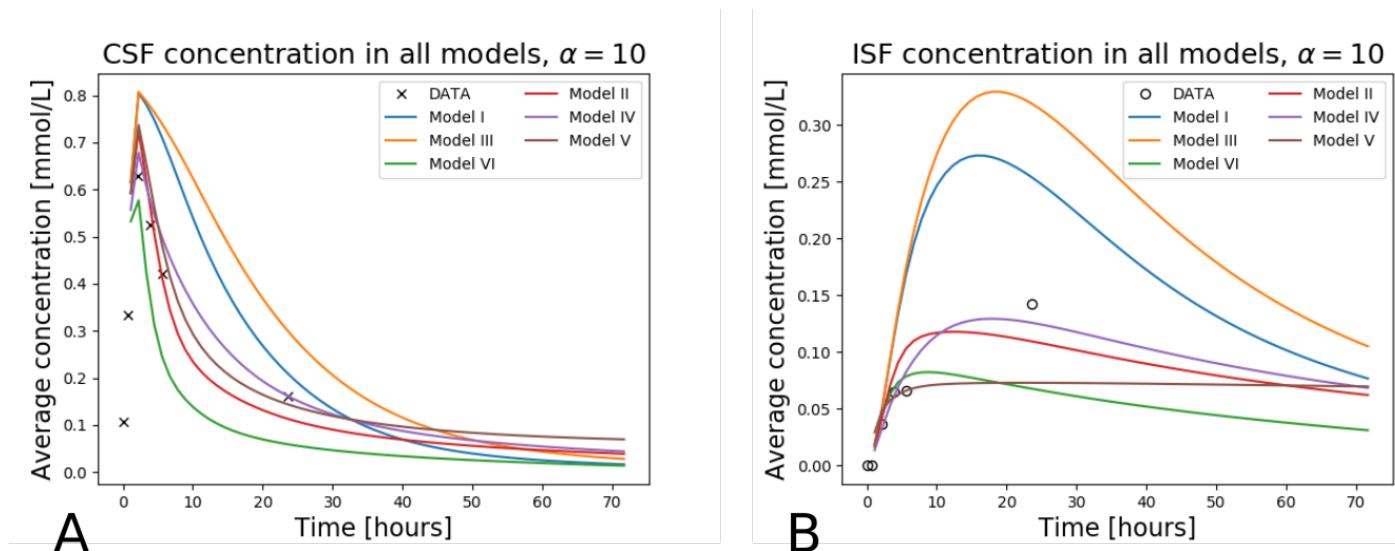


Figure 5. The figure shows concentration in the CSF (A) and the ISF (A) for all models over one week. The tracer concentration data from T1 MR images for this patient is also shown.

194 After one week, a some tracer are still found within the brain, slowly diffusing back towards the pial surface for
195 clearance via convection in the SAS (data not shown). Models I and III (with outflow via the parasagittal dura) are
196 the only models where tracer reaches the upper convexities of the brain, resulting in a brain wide distribution of
197 tracers. In Model III, where a diffusive molecular resistance is added at the parasagittal dura, tracer accumulates
198 near the outflux region (4B, Model III).

199 Model V is the only model where tracer reaches the ventricular system, while Model IV has localized accumula-
200 tion of tracers around the brain stem. Model VI, with increased CSF production, show generally lower concentration
201 of tracers, and some accumulation near the outflux route at the cribriform plate.

202 The average concentration over time for all models, and $\alpha = 10$, is compared in Figure 5, both for the ISF and
203 CSF. The figure also contains in vivo concentration estimates in both spaces. We observe that a combination of the
204 different outflow routes, i.e. Model I and V, gives a comparable result to that of the MR images. Model I and III
205 both display higher concentrations than the data in both the CSF and parenchyma/ISF (Figure 5). Model II, IV and
206 V, on the other hand, yield the comparable or lower concentrations.

207 3.6 Clearance rates induced by CSF circulation and dispersion

208 Model I and II both display high three-day clearance rates for all dispersion factors (Figure 6A-B). Specifically, the
209 three day clearance rates are between 94.1 and 97.7 % for Model I and between 88.9 and 94.9 % for Model II (Table
210 2). The tracer concentration is initially higher in the SAS allowing for diffusive influx to the brain. At later time
211 points, the SAS has been cleared, mainly via convective flow, and the tracer partly remains inside the parenchyma,
212 delaying the total clearance of tracers from the intracranial compartment. Model I has slightly higher peak average
213 parenchyma concentration values than Model II, reaching 0.30 and 0.24 mmol/L, respectively. The time to peak in
214 the parenchyma occurred after 7.8 – 19.0 hours for Model I and 10.1 – 16.8 hours or Model II.

215 For the models including a molecular resistance to outflow at the outflow site (i.e. Model III and IV), the three
216 day clearance rate is comparable to Models I and II, except for the case when $\alpha = 1000$ in model III (Table 2).
217 The highest three day clearance is obtained with $\alpha = 1$ for both Model III and IV (95.7 and 99.0 % clearance,
218 respectively). The lowest three day clearance is obtained with $\alpha = 1000$ for model III (36.3 % clearance) and $\alpha = 10$
219 for model IV (89.5 % clearance, Table 2). Model III reaches a peak parenchyma concentration of 0.50 mmol/L,
220 while Model IV have a lower peak of 0.23 mmol/L. The time to peak exceeds 19.0 hours for all dispersion factors in
221 Model III, which is much later than the other α s. Model IV on the other hand peaks between 11.2 and 17.9
222 hours.

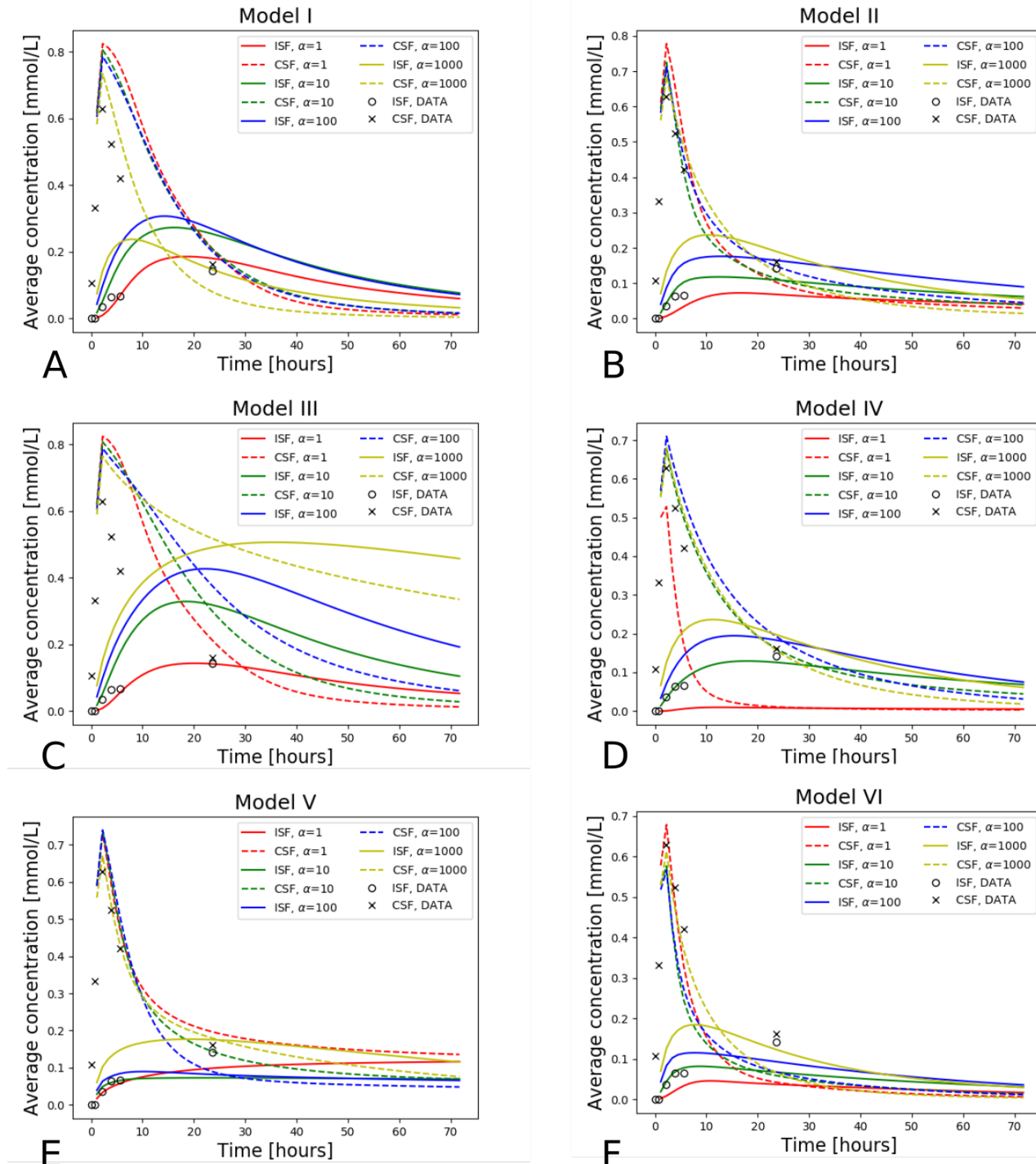


Figure 6. Average concentration in the parenchyma (par.) and CSF over a period of 72 hours. Models I-VI is used with dispersion values $\alpha = 1, 10, 100, 1000$. Also plotted is the concentration data taken from T1-weighted images of this specific patient as a ground truth. The tracer injection (present from 0 to 2.24 hours) is seen as a sharp increase in CSF concentration at early time points. When the injection is no longer present, the total amount of tracers within the intracranial compartment starts decreasing. The tracer concentration data from T1 contrast enhanced images for the patient is also included. (A) Model I, (B) Model II, (C) Model III, (D) Model IV, (E) Model V and (F) Model VI.

223 **3.7 Clearance of gadobutrol with reverse pathways**

224 Model V (with reversal of CSF flow in the aqueduct) results in low parenchymal enrichment compared to Models
225 I–IV (Table 2, Figure 6E). The three day clearance rate is between 75.1 and 90.0 % depending on α and the
226 peak average concentration is 0.18 mmol/L in the parenchyma (Table 2). The time to peak concentration in the
227 parenchyma is long for $\alpha = 1$, occurring later than after 1 week, but for larger dispersion factors, the peak occurs
228 between 10.8 and 22.4 hours.

229 **3.8 Increased CSF production results in rapid clearance**

230 Model VI, with double the CSF production of the other models, displayed rapid clearance from the CSF (Figure 6F).
231 The rapid turnover of CSF limited the influx and facilitated clearance also within the parenchyma. The three day
232 clearance rate for all dispersion factors ranged between 95.4 – 97.9 % (Table 2). The peak average parenchyma
233 concentration occurs early, between 7.8 and 11.2 hours and reaches at most 0.15 mmol/L, when $\alpha = 1000$.

234 **4 Discussion**

235 In this paper we have simulated molecular transport by diffusion and convection for six different models investigating
236 distribution of gadobutrol molecules entering the intracranial compartment via the foramen magnum. The different
237 models represent different outflow routes, and CSF flow patterns vary considerably between models. The effect of
238 outflow route and dispersion factor modify the distribution and clearance patterns in a non-linear and unpredictable
239 manner. Outflow through either the parasagittal dura, the cribriform plate or through meningeal lymphatics, typically
240 cleared 80–99% of injected tracers over a time period of three days. These three models however, display very
241 different spatial distribution of tracers. In Models I and III tracer distributes more or less throughout the frontal
242 cortex, while when outflow occurs through meningeal lymphatics, tracers are mainly located at the brain stem at the
243 base of the brain.

244 With a daily production of 0.5 and 1.0 L/day in our models, the velocity reaches 10 and 17.8 mm/s in the
245 aqueduct. Pulsatile aqueductal flow velocities of several cm/s have been measured experimentally^{48–50} in the range
246 1–10 cm/s. Average velocities max velocities were reported around 5 cm/s, corresponding to a total volume flux of
247 0.3 mL per cycle, of which 0.01 mL was net^{4,32}. As the net flow is around 1/30 of the total flux, the corresponding
248 net max velocity can then be estimated as 5/30 cm/s, somewhat below the velocities estimated here. Further, in
249 iNPH patients it has been reported Phase-contrast MR has reported retro-grade net flow in the aqueduct⁴. Model V
250 is motivated by retro-grade aqueductal flow and we see that this model is distinct from the other models in that there
251 is significant ventricular enrichment, as often seen in iNPH¹⁵.

252 On the pial surface of the brain, we observe velocities up to 20 – 50 $\mu\text{m/s}$ in models I–IV, and up to 100 $\mu\text{m/s}$ in
253 model VI. These velocities align relatively well with experimentally observed bulk flow velocities of around 20
254 $\mu\text{m/s}$ observed in mice^{8,9}. Thus, CSF flow observed in these studies, may very well be a result of CSF production
255 and absorption, driven by small static pressure differences. It should be noted that mice have approximately 3x faster
256 CSF turnover compared to humans³⁶. Given otherwise similar CSF dynamics between the species, one would thus
257 expect CSF production to cause higher velocities at the surface of the mouse brain compared to a human. Comparing
258 model II and model VI, the increased CSF efflux to the cribriform plate limits tracer influx to the brain, in line with
259 the hypothesis of Ma et al.⁷. We observe that models with a short distance between injection and absorption site
260 (models II, IV and V) limits the influx of tracers to the parenchyma. In general, tracers will enter the brain if present
261 on the surface over a long time period. For a given tracer, the amount of tracers entering the brain will thus be
262 affected by both the CSF velocity and the distance from the injection site to the absorption site.

263 Gadobutrol injections has been studied in human subjects in several papers. Eide, Ringstad and colleagues have
264 reported MR intensity increase for a large number of subjects^{6,15,22,35}, while Watts et al⁵¹ quantified gadobutrol
265 concentrations over time in a single patient. These studies show an initial sharp increase in tracer concentration in
266 the SAS, typically reaching a peak at around 2–6 hours. In the parenchyma, peak values occur between 10 and 24
267 hours, depending on the region of interest. Gray matter regions, closer to the pial surface typically peak at around 10
268 hours, while for specific white matter regions, peak values may occur closer to 24–40 hours post-injection^{15,51}. In
269 all our models, peak CSF concentration occurs at the time when the gadobutrol influx at the foramen magnum is

270 turned off, i.e. after approximately 2 hours. More interestingly, the ISF concentration peaks later, and the time to
271 peak is between 10 and 20 hours in 15 out of 24 models tested. ISF concentration is reported to decay relatively
272 slow, with an approximate concentration at 48 hours at half its peak value²². Furthermore, the peak concentration
273 of gadobutrol has been measured as 0.5 mmol/L in the CSF and around 0.12 mmol/L in the ISF⁵¹, in line with
274 both the estimates of observed concentration the iNPH patient and the results from our models. Both Model II
275 (outflow through the cribriform plate) and Model IV (outflow via meningeal lymphatics) match all these criteria
276 well when the dispersion in the SAS was modeled by $\alpha = 10$. Model I (outflow through the parasagittal dura)
277 replicate experimentally observed ISF concentration without additional dispersion in the SAS, but clearance from
278 the SAS is delayed in this model compared to experimental data. With a molecular resistance to outflow on the
279 parasagittal dura (Model III), simulations reproduce accumulation of tracers in this region, but clearance kinetics
280 are slower than expected. With a doubling of CSF production (Model VI) the kinetics of ISF and CSF clearance is
281 faster than expected for all dispersion factors tested. In the model with reversed flow in the aqueduct (Model V),
282 we qualitatively reproduce the tracer enhancement in the aqueduct as seen in iNPH patients⁶. However, rapid flow
283 through the aqueduct and into the choroid plexus prevents the expected brain-wide enhancement of tracer¹⁵, and in
284 Model V tracers are confined to the foramen magnum or in the vicinity of the lateral ventricles. Combined, these
285 results suggest that a combination of production and efflux sites may be needed to reproduce the observed tracer
286 distribution^{6,15,22}.

287 The role of different outflow routes from the SAS have been debated and challenged over years. In particular,
288 the traditional view of outflow predominately through arachnoid granulations has been criticized recently². Our
289 Model I is conceptually similar to outflow through arachnoid granulations with CSF draining close to the dural sinus.
290 The results from our simulations can not exclude any of the proposed major outflow routes, as all of them resemble
291 experimental data in at least some measure. A specific weighting between inflow and outflow routes may potentially
292 be sufficient to explain differences between groups (e.g. iNPH vs control), or differences between individuals. The
293 results do show unequivocally that CSF flow and clearance is a major player in CNS clearance. Convective flow in
294 the SAS speeds up intracranial clearance from years to hours and days, an enormous effect compared to the effect of
295 bulk flow of around 1 $\mu\text{m/s}$ within the ECS²⁷. Furthermore, changes in the dispersion factor (increased diffusion due
296 to mixing) only in the SAS changed both peak values and clearance rates within the brain ECS.

297 In terms of limitations, we only performed the simulations on a single patient. To create one patient specific
298 mesh with high mesh quality that includes all anatomical regions of interest was time consuming, and increasing the
299 amount of subjects was not the scope of this study. Similarly, as the initial mesh already consisted of nearly 7M
300 cells, a mesh resolution study was not performed. Based on previous simulation studies²⁷, using similar number of
301 cells, we believe the mesh is sufficiently resolved. To resolve all regions of the SAS, the SAS was expanded by 1
302 mm. This modification increases the volume of which fluid flows, and thus slightly reduce velocities we find in the
303 SAS. The total CSF volume was increased by around 33%, we thus assume that our reported SAS flow velocities of
304 20–50 $\mu\text{m/s}$ are lower estimates. In the SAS, we assumed that the dispersion factor were similar in all subregions.
305 In reality, dispersion would be expected to be enhanced close to larger arteries³⁵ and in regions where pulsatile CSF
306 flow is substantial (e.g. near the foramen magnum). Furthermore, we did not include ISF velocities in the foramen
307 magnum. There is very little knowledge exactly on how the velocity fields are directed²⁷, especially without a priori
308 knowledge of the location of blood vessels. In addition, the purpose of this study was to assess the effect of SAS
309 convection, independent of potential bulk flow within the brain. Finally, we should note that we assumed that all
310 injected gadobutrol reached the foramen magnum, while around 33 % of CSF has been proposed to be drained along
311 the spinal canal⁵². The latter point may explain the fact that most of the reasonable models tested (Model I, II and
312 IV) all generally display a slight overestimation of the SAS peak concentration in our models compared to the data.

313 In conclusion we have demonstrated that convection in the SAS yield rapid clearance both from the SAS and the
314 ISF, even when pure diffusive transport were assumed in the ECS. Convective fluid flow in the SAS has the potential
315 to speed up clearance from years (as would be the case for purely diffusive transport) to days. As none of the models
316 tested were able to reproduce the observed data perfectly (both qualitatively and quantitatively), a combination of
317 the different outflow routes seem most plausible, and their relative weight may differ between groups⁶.

318 **Conflict of Interest Statement**

319 The authors declare that the research was conducted in the absence of any commercial or financial relationships that
320 could be construed as a potential conflict of interest.

321 **Author Contributions**

322 M.H., V.V., L.M.V., P.K.E, G.R., M.E.R. and K.A.M. conceived the simulations, L.M.V. and M.H. segmented and
323 meshed MR images, M.H. conducted the simulations, V.V. M.H. and L.M.V did the analysis of the results and M.H.
324 made the figures. All authors discussed the simulations and results. M.H., V.V, L.M.V., M.E.R. and K.A.M. wrote
325 the first draft. All authors revised and approved the final manuscript.

326 **Funding**

327 K.A.M. acknowledges support from the Research Council of Norway, grant 300305 and 301013 and the national
328 infrastructure for computational science in Norway, Sigma2, grant NN9279K. M.E.R. has received funding from the
329 European Research Council (ERC) under the European Union's Horizon 2020 research and innovation programme
330 under grant agreement 714892.

331 **References**

- 332 **1.** Abbott, N. J., Pizzo, M. E., Preston, J. E., Janigro, D. & Thorne, R. G. The role of brain barriers in fluid
333 movement in the cns: is there a 'glymphatic' system? *Acta neuropathologica* **135**, 387–407 (2018).
- 334 **2.** Proulx, S. T. Cerebrospinal fluid outflow: a review of the historical and contemporary evidence for arachnoid
335 villi, perineural routes, and dural lymphatics. *Cell. Mol. Life Sci.* 1–29 (2021).
- 336 **3.** Weed, L. H. Studies on cerebro-spinal fluid. no. iv: the dual source of cerebro-spinal fluid. *The J. medical*
337 *research* **31**, 93 (1914).
- 338 **4.** Lindstrøm, E. K., Ringstad, G., Mardal, K.-A. & Eide, P. K. Cerebrospinal fluid volumetric net flow rate and
339 direction in idiopathic normal pressure hydrocephalus. *NeuroImage: Clin.* **20**, 731–741 (2018).
- 340 **5.** Lindstrøm, E. K. *et al.* Magnitude and direction of aqueductal cerebrospinal fluid flow: large variations in
341 patients with intracranial aneurysms with or without a previous subarachnoid hemorrhage. *Acta neurochirurgica*
342 **161**, 247–256 (2019).
- 343 **6.** Eide, P. K., Valnes, L. M., Pripp, A. H., Mardal, K.-A. & Ringstad, G. Delayed clearance of cerebrospinal fluid
344 tracer from choroid plexus in idiopathic normal pressure hydrocephalus. *J. Cereb. Blood Flow & Metab.* **40**,
345 1849–1858 (2020).
- 346 **7.** Ma, Q. *et al.* Rapid lymphatic efflux limits cerebrospinal fluid flow to the brain. *Acta neuropathologica* **137**,
347 151–165 (2019).
- 348 **8.** Bedussi, B., Almasian, M., de Vos, J., VanBavel, E. & Bakker, E. N. Paravascular spaces at the brain surface:
349 Low resistance pathways for cerebrospinal fluid flow. *J. Cereb. Blood Flow & Metab.* **38**, 719–726 (2018).
- 350 **9.** Mestre, H. *et al.* Flow of cerebrospinal fluid is driven by arterial pulsations and is reduced in hypertension. *Nat.*
351 *communications* **9**, 1–9 (2018).
- 352 **10.** Vinje, V., Eklund, A., Mardal, K.-A., Rognes, M. E. & Støverud, K.-H. Intracranial pressure elevation alters csf
353 clearance pathways. *Fluids Barriers CNS* **17**, 1–19 (2020).
- 354 **11.** Ma, Q., Ineichen, B. V., Detmar, M. & Proulx, S. T. Outflow of cerebrospinal fluid is predominantly through
355 lymphatic vessels and is reduced in aged mice. *Nat. communications* **8**, 1–13 (2017).
- 356 **12.** Louveau, A. *et al.* Understanding the functions and relationships of the glymphatic system and meningeal
357 lymphatics. *The J. clinical investigation* **127**, 3210–3219 (2017).

- 358 **13.** Iliff, J. J. *et al.* A paravascular pathway facilitates csf flow through the brain parenchyma and the clearance of
359 interstitial solutes, including amyloid β . *Sci. translational medicine* **4**, 147ra111–147ra111 (2012).
- 360 **14.** Hladky, S. B. & Barrand, M. A. Mechanisms of fluid movement into, through and out of the brain: evaluation
361 of the evidence. *Fluids Barriers CNS* **11**, 1–32 (2014).
- 362 **15.** Ringstad, G. *et al.* Brain-wide glymphatic enhancement and clearance in humans assessed with mri. *JCI insight*
363 **3** (2018).
- 364 **16.** Schubert, J. J. *et al.* Dynamic 11c-pib pet shows cerebrospinal fluid flow alterations in alzheimer disease and
365 multiple sclerosis. *J. Nucl. Medicine* **60**, 1452–1460 (2019).
- 366 **17.** Tarasoff-Conway, J. M. *et al.* Clearance systems in the brain—implications for alzheimer disease. *Nat. reviews*
367 *neurology* **11**, 457–470 (2015).
- 368 **18.** Thal, D. R., Griffin, W. S. T., de Vos, R. A. & Ghebremedhin, E. Cerebral amyloid angiopathy and its relationship
369 to alzheimer’s disease. *Acta neuropathologica* **115**, 599–609 (2008).
- 370 **19.** Zeppenfeld, D. M. *et al.* Association of perivascular localization of aquaporin-4 with cognition and alzheimer
371 disease in aging brains. *JAMA neurology* **74**, 91–99 (2017).
- 372 **20.** Shokri-Kojori, E. *et al.* β -amyloid accumulation in the human brain after one night of sleep deprivation. *Proc.*
373 *Natl. Acad. Sci.* **115**, 4483–4488 (2018).
- 374 **21.** Xie, L. *et al.* Sleep drives metabolite clearance from the adult brain. *science* **342**, 373–377 (2013).
- 375 **22.** Eide, P. K., Vinje, V., Pripp, A. H., Mardal, K.-A. & Ringstad, G. Sleep deprivation impairs molecular clearance
376 from the human brain. *Brain* **144**, 863–874 (2021).
- 377 **23.** Asgari, M., De Zélicourt, D. & Kurtcuoglu, V. Glymphatic solute transport does not require bulk flow. *Sci.*
378 *reports* **6**, 1–11 (2016).
- 379 **24.** Smith, A. J. & Verkman, A. S. The “glymphatic” mechanism for solute clearance in alzheimer’s disease: game
380 changer or unproven speculation? *The FASEB J.* **32**, 543–551 (2018).
- 381 **25.** Mestre, H. *et al.* Aquaporin-4-dependent glymphatic solute transport in the rodent brain. *Elife* **7**, e40070 (2018).
- 382 **26.** Ray, L., Iliff, J. J. & Heys, J. J. Analysis of convective and diffusive transport in the brain interstitium. *Fluids*
383 *Barriers CNS* **16**, 1–18 (2019).
- 384 **27.** Croci, M., Vinje, V. & Rognes, M. E. Uncertainty quantification of parenchymal tracer distribution using
385 random diffusion and convective velocity fields. *Fluids Barriers CNS* **16**, 1–21 (2019).
- 386 **28.** Valnes, L. M. *et al.* Apparent diffusion coefficient estimates based on 24 hours tracer movement support
387 glymphatic transport in human cerebral cortex. *Sci. reports* **10**, 1–12 (2020).
- 388 **29.** Ray, L. A., Pike, M., Simon, M., Iliff, J. J. & Heys, J. J. Quantitative analysis of macroscopic solute transport in
389 the murine brain. *Fluids Barriers CNS* **18**, 1–19 (2021).
- 390 **30.** Kohn, M. I. *et al.* Analysis of brain and cerebrospinal fluid volumes with mr imaging. part i. methods, reliability,
391 and validation. *Radiology* **178**, 115–122 (1991).
- 392 **31.** Yamada, S., Ishikawa, M. & Yamamoto, K. Comparison of csf distribution between idiopathic normal pressure
393 hydrocephalus and alzheimer disease. *Am. J. Neuroradiol.* **37**, 1249–1255 (2016).
- 394 **32.** Eide, P. K., Valnes, L. M., Lindstrøm, E. K., Mardal, K.-A. & Ringstad, G. Direction and magnitude of
395 cerebrospinal fluid flow vary substantially across central nervous system diseases. *Fluids Barriers CNS* **18**,
396 1–18 (2021).
- 397 **33.** Bradley, W. G., Haughton, V. & Mardal, K.-A. Cerebrospinal fluid flow in adults. In *Handbook of Clinical*
398 *Neurology*, vol. 135, 591–601 (Elsevier, 2016).
- 399 **34.** Vinje, V. *et al.* Respiratory influence on cerebrospinal fluid flow—a computational study based on long-term
400 intracranial pressure measurements. *Sci. reports* **9**, 1–13 (2019).

- 401 **35.** Ringstad, G., Vatnehol, S. A. S. & Eide, P. K. Glymphatic mri in idiopathic normal pressure hydrocephalus.
402 *Brain* **140**, 2691–2705 (2017).
- 403 **36.** Pardridge, W. M. Csf, blood-brain barrier, and brain drug delivery. *Expert. opinion on drug delivery* **13**, 963–975
404 (2016).
- 405 **37.** Ringstad, G. & Eide, P. K. Cerebrospinal fluid tracer efflux to parasagittal dura in humans. *Nat. communications*
406 **11**, 1–9 (2020).
- 407 **38.** Fischl, B. Freesurfer. *Neuroimage* **62**, 774–781 (2012).
- 408 **39.** SVMTK. SurfaceVolumeMeshingToolKit (2021). Original-date: 2017-09-22T15:36:28Z.
- 409 **40.** Daversin-Catty, C., Vinje, V., Mardal, K.-A. & Rognes, M. E. The mechanisms behind perivascular fluid flow.
410 *Plos one* **15**, e0244442 (2020).
- 411 **41.** Nilsson, C., Stahlberg, F., Gideon, P., Thomsen, C. & Henriksen, O. The nocturnal increase in human
412 cerebrospinal fluid production is inhibited by a beta 1-receptor antagonist. *Am. J. Physiol. Integr. Comp. Physiol.*
413 **267**, R1445–R1448 (1994).
- 414 **42.** Nilsson, C. *et al.* Circadian variation in human cerebrospinal fluid production measured by magnetic resonance
415 imaging. *Am. J. Physiol. Integr. Comp. Physiol.* **262**, R20–R24 (1992).
- 416 **43.** Sharp, M. K., Carare, R. O. & Martin, B. A. Dispersion in porous media in oscillatory flow between flat plates:
417 applications to intrathecal, periarterial and paraarterial solute transport in the central nervous system. *Fluids*
418 *Barriers CNS* **16**, 1–17 (2019).
- 419 **44.** Nicholson, C. & Phillips, J. Ion diffusion modified by tortuosity and volume fraction in the extracellular
420 microenvironment of the rat cerebellum. *The J. physiology* **321**, 225–257 (1981).
- 421 **45.** Logg, A., Mardal, K.-A. & Wells, G. *Automated solution of differential equations by the finite element method:*
422 *The FEniCS book*, vol. 84 (Springer Science & Business Media, 2012).
- 423 **46.** Alnæs, M. *et al.* The fenics project version 1.5. *Arch. Numer. Softw.* **3** (2015).
- 424 **47.** Taylor, A. J., Salerno, M., Dharmakumar, R. & Jerosch-Herold, M. T1 mapping: basic techniques and clinical
425 applications. *JACC: Cardiovasc. Imaging* **9**, 67–81 (2016).
- 426 **48.** Lee, J. H. *et al.* Csf flow quantification of the cerebral aqueduct in normal volunteers using phase contrast cine
427 mr imaging. *Korean journal radiology* **5**, 81–86 (2004).
- 428 **49.** Tawfik, A. M., Elsorogy, L., Abdelghaffar, R., Naby, A. A. & Elmenshawi, I. Phase-contrast mri csf flow
429 measurements for the diagnosis of normal-pressure hydrocephalus: observer agreement of velocity versus
430 volume parameters. *Am. J. Roentgenol.* **208**, 838–843 (2017).
- 431 **50.** Spijkerman, J. M. *et al.* Phase contrast mri measurements of net cerebrospinal fluid flow through the cerebral
432 aqueduct are confounded by respiration. *J. Magn. Reson. Imaging* **49**, 433–444 (2019).
- 433 **51.** Watts, R., Steinklein, J., Waldman, L., Zhou, X. & Filippi, C. Measuring glymphatic flow in man using
434 quantitative contrast-enhanced mri. *Am. J. Neuroradiol.* **40**, 648–651 (2019).
- 435 **52.** Edsbacke, M., Tisell, M., Jacobsson, L. & Wikkelso, C. Spinal csf absorption in healthy individuals. *Am. J.*
436 *Physiol. Integr. Comp. Physiol.* **287**, R1450–R1455 (2004).